Prepared for submission to JCAP

Seasonal Variation of the Underground Cosmic Muon Flux Observed at Daya Bay

F. P. An[a] A. B. Balantekin[b] H. R. Band[c] M. Bishai[d] S. Blyth[e,f] D. Cao[g] G. F. Cao[h] J. Cao[h] Y. L. Chan[i] J. F. Chang[h] Y. Chang[f] H. S. Chen[h] Q. Y. Chen[j] S. M. Chen[k] Y. X. Chen[l] Y. Chen[m] J. Cheng[j] Z. K. Cheng[n] J. J. Cherwinka[b] M. C. Chu[i] A. Chukanov[o] J. P. Cummings[p] Y. Y. Ding[h] M. V. Diwan[d] M. Dolgareva[o] J. Dove[q] D. A. Dwyer[r] W. R. Edwards[r] R. Gill[d] M. Gonchar[o] G. H. Gong[k] H. Gong[k] M. Grassi[h] W. Q. Gu[s] L. Guo[k] X. H. Guo[t] Y. H. Guo[u] Z. Guo[k] R. W. Hackenburg[d] S. Hans[d,1] M. He[h] K. M. Heeger[c] Y. K. Heng[h] A. Higuera[w] Y. B. Hsiung[e] B. Z. Hu[e] T. Hu[h] E. C. Huang[q] H. X. Huang[x] X. T. Huang[j] P. Huber[y] W. Huo[z] G. Hussain[k] D. E. Jaffe[d] K. L. Jen[aa] S. Jetter[h] X. P. Ji[ab,k] X. L. Ji[h] J. B. Jiao[j] R. A. Johnson[ac] D. Jones[ad] L. Kang[ae] S. H. Kettell[d] A. Khan[n] S. Kohn[af] M. Kramer[r,af] K. K. Kwan[i] M. W. Kwok[i] T. Kwok[ag] T. J. Langford[c] K. Lau[w] L. Lebanowski[k] J. Lee[r] J. H. C. Lee[ag] R. T. Lei[ae] R. Leitner[ah] C. Li[j] D. J. Li[z] F. Li[h] G. S. Li[s] Q. J. Li[h] S. Li[ae] S. C. Li[y] W. D. Li[h] X. N. Li[h] X. Q. Li[ab] Y. F. Li[h] Z. B. Li[n] H. Liang[z] C. J. Lin[r] G. L. Lin[aa] S. Lin[ae] S. K. Lin[w] Y.-C. Lin[e] J. J. Ling[n] J. M. Link[y] L. Littenberg[d] B. R. Littlejohn[ai] J. L. Liu[s] J. C. Liu[h] C. W. Loh[g] C. Lu[aj] H. Q. Lu[h] J. S. Lu[h] K. B. Luk[af,r] X. Y. Ma[h] X. B. Ma[l] Y. Q. Ma[h] Y. Malyshkin[ak] D. A. Martinez Caicedo[ai] K. T. McDonald[aj] R. D. McKeown[al,am] I. Mitchell[w] Y. Nakajima[r] J. Napolitano[ad] D. Naumov[o] E. Naumova[o] H. Y. Ngai[ag] J. P. Ochoa-Ricoux[ak] A. Olshevskiy[o] H.-R. Pan[e] J. Park[y] S. Patton[r] V. Pec[ah] J. C. Peng[q] L. Pinsky[w] C. S. J. Pun[ag] F. Z. Qi[h] M. Qi[g] X. Qian[d] R. M. Qiu[l] N. Raper[an,n] J. Ren[x] R. Rosero[d] B. Roskovec[ah] X. C. Ruan[x] C. Sebastiani[h] H. Steiner[af,r] J. L. Sun[ao] W. Tang[d]

[1]Now at: Department of Chemistry and Chemical Technology, Bronx Community College, Bronx, New York 10453

arXiv:1708.01265v1 [physics.ins-det] 3 Aug 2017

**D. Taychenachev[o] K. Treskov[o] K. V. Tsang[r] C. E. Tull[r]
N. Viaux[ak] B. Viren[d] V. Vorobel[ah] C. H. Wang[f] M. Wang[j]
N. Y. Wang[t] R. G. Wang[h] W. Wang[am,n] X. Wang[ap]
Y. F. Wang[h] Z. Wang[k] Z. Wang[h] Z. M. Wang[h] H. Y. Wei[k]
L. J. Wen[h] K. Whisnant[aq] C. G. White[ai] L. Whitehead[w]
H. L. H. Wong[af,r] S. C. F. Wong[n] E. Worcester[d] C.-H. Wu[aa]
Q. Wu[j] W. J. Wu[h] D. M. Xia[ar] J. K. Xia[h] Z. Z. Xing[h] J. L. Xu[h]
Y. Xu[n] T. Xue[k] C. G. Yang[h] H. Yang[g] L. Yang[ae] M. S. Yang[h]
M. T. Yang[j] M. Ye[h] Z. Ye[w] M. Yeh[d] B. L. Young[aq] Z. Y. Yu[h]
S. Zeng[h] L. Zhan[h] C. Zhang[d] C. C. Zhang[h] H. H. Zhang[n]
J. W. Zhang[h] Q. M. Zhang[u] X. T. Zhang[h] Y. M. Zhang[k]
Y. X. Zhang[ao] Y. M. Zhang[n] Z. J. Zhang[ae] Z. Y. Zhang[h]
Z. P. Zhang[z] J. Zhao[h] L. Zhou[h] H. L. Zhuang[h] J. H. Zou[h]**

[a]Institute of Modern Physics, East China University of Science and Technology, Shanghai
[b]University of Wisconsin, Madison, Wisconsin 53706
[c]Wright Laboratory and Department of Physics, Yale University, New Haven, Connecticut 06520
[d]Brookhaven National Laboratory, Upton, New York 11973
[e]Department of Physics, National Taiwan University, Taipei
[f]National United University, Miao-Li
[g]Nanjing University, Nanjing
[h]Institute of High Energy Physics, Beijing
[i]Chinese University of Hong Kong, Hong Kong
[j]Shandong University, Jinan
[k]Department of Engineering Physics, Tsinghua University, Beijing
[l]North China Electric Power University, Beijing
[m]Shenzhen University, Shenzhen
[n]Sun Yat-Sen (Zhongshan) University, Guangzhou
[o]Joint Institute for Nuclear Research, Dubna, Moscow Region
[p]Siena College, Loudonville, New York 12211
[q]Department of Physics, University of Illinois at Urbana-Champaign, Urbana, Illinois 61801
[r]Lawrence Berkeley National Laboratory, Berkeley, California 94720
[s]Department of Physics and Astronomy, Shanghai Jiao Tong University, Shanghai Laboratory for Particle Physics and Cosmology, Shanghai
[t]Beijing Normal University, Beijing
[u]Department of Nuclear Science and Technology, School of Energy and Power Engineering, Xi'an Jiaotong University, Xi'an
[w]Department of Physics, University of Houston, Houston, Texas 77204
[x]China Institute of Atomic Energy, Beijing
[y]Center for Neutrino Physics, Virginia Tech, Blacksburg, Virginia 24061
[z]University of Science and Technology of China, Hefei
[aa]Institute of Physics, National Chiao-Tung University, Hsinchu

[ab]School of Physics, Nankai University, Tianjin
[ac]Department of Physics, University of Cincinnati, Cincinnati, Ohio 45221
[ad]Department of Physics, College of Science and Technology, Temple University, Philadelphia, Pennsylvania 19122
[ae]Dongguan University of Technology, Dongguan
[af]Department of Physics, University of California, Berkeley, California 94720
[ag]Department of Physics, The University of Hong Kong, Pokfulam, Hong Kong
[ah]Charles University, Faculty of Mathematics and Physics, Prague
[ai]Department of Physics, Illinois Institute of Technology, Chicago, Illinois 60616
[aj]Joseph Henry Laboratories, Princeton University, Princeton, New Jersey 08544
[ak]Instituto de Física, Pontificia Universidad Católica de Chile, Santiago
[al]California Institute of Technology, Pasadena, California 91125
[am]College of William and Mary, Williamsburg, Virginia 23187
[an]Department of Physics, Applied Physics, and Astronomy, Rensselaer Polytechnic Institute, Troy, New York 12180
[ao]China General Nuclear Power Group, Shenzhen
[ap]College of Electronic Science and Engineering, National University of Defense Technology, Changsha
[aq]Iowa State University, Ames, Iowa 50011
[ar]Chongqing University, Chongqing

Abstract. The Daya Bay Experiment consists of eight identically designed detectors located in three underground experimental halls named as EH1, EH2, EH3, with 250, 265 and 860 meters of water equivalent vertical overburden, respectively. Cosmic muon events have been recorded over a two-year period. The underground muon rate is observed to be positively correlated with the effective atmospheric temperature and to follow a seasonal modulation pattern. The correlation coefficient α, describing how a variation in the muon rate relates to a variation in the effective atmospheric temperature, is found to be $\alpha_{\mathrm{EH1}} = 0.362 \pm 0.031$, $\alpha_{\mathrm{EH2}} = 0.433 \pm 0.038$ and $\alpha_{\mathrm{EH3}} = 0.641 \pm 0.057$ for each experimental hall.

Contents

1 Introduction

Early investigations into the nature and origin of cosmic rays included searches for correlations between the penetrating component of the cosmic ray flux and atmospheric variables [1]. We now know that this penetrating component is composed of positive and negative muons. The muons result from the decay of charged mesons produced by interactions of primary cosmic rays with the upper atmosphere. Furthermore, a number of experiments have observed the underground muon intensity to be positively correlated with the atmospheric temperature [1–19]. As the temperature increases, the atmosphere becomes less dense, and the probability for a meson to interact with molecules in the atmosphere is reduced. The corresponding increase in meson decays yields a larger muon intensity over the summer months. The great majority of the experimental results are reported in terms of α, the correlation coefficient between the muon flux and the atmospheric temperature. This coefficient increases as a function of overburden, and hence Daya Bay, with three underground experimental halls at different depths, is an ideal setup to perform such a measurement.

2 Daya Bay Experiment

Daya Bay is designed to measure the previously unknown value of the neutrino mixing angle θ_{13} by measuring the survival probability of electron antineutrinos from nuclear reactors at suitable distances. Electron antineutrinos are detected via inverse beta decay (IBD) $\bar{\nu}_e p \rightarrow e^+ n$ where the positron energy is less than 10 MeV for reactor antineutrinos. Figure 1 shows a diagram of the Daya Bay experimental site. The Daya Bay Nuclear Power Plant complex consists of six reactors. The experiment uses eight identically designed antineutrino detectors

Hall	Overburden		Muon flux
	m	mwe	Hz/m^2
EH1	93	250	1.16 ± 0.11
EH2	100	265	0.86 ± 0.09
EH3	324	860	0.054 ± 0.006

Table 1. Vertical overburden and measured muon flux at the three experimental halls [21].

(ADs) located in three underground experimental halls (EHs). Two halls, EH1 and EH2, are located near the reactor cores, while the last hall, EH3, is located farther away at a distance optimized to measure θ_{13} through neutrino oscillation. Daya Bay began operations in December 2011 with six ADs: two in EH1, one in EH2, and three in EH3. In Summer 2012, the remaining two ADs were installed, one in EH2 and the other one in EH3, and operations began with all eight ADs. The vertical overburden and the measured muon flux at each EH are listed in Table 1.

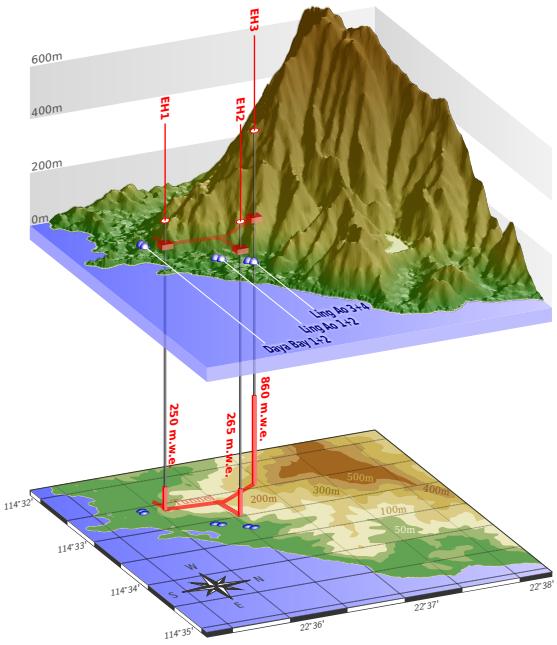

Figure 1. Location of the Nuclear Power Plants and of the Experimental halls, together with the elevation profile of the mountain above the experimental halls.

The ADs at each hall are contained inside a muon detector system, which consists of a two-zone pure water Cherenkov detector, referred to as the inner and outer water shields (IWS and OWS), covered on top by an array of resistive plate chambers (RPCs). The water pool is designed so that at least 2.5 m of water surrounds each AD in every direction. There are a total of 288 water pool PMTs at each of the near sites (EH1, EH2) and 384 PMTs at EH3, distributed in the inner and outer regions, which are optically separated by Tyvek sheets. Each AD consists of three nested cylindrical volumes separated by transparent acrylic vessels. The inner acrylic vessel (IAV) has a 3.1-m diameter and is filled with 20 tons of 0.1% gadolinium-doped liquid scintillator (GdLS) as the primary antineutrino target. The 4-m diameter outer acrylic vessel (OAV) surrounding the target is filled with about 21 tons of undoped liquid scintillator (LS), increasing the efficiency of detecting gamma rays produced in the GdLS region. The outermost stainless steel vessel has a diameter of 5 m and is filled with 37 tons of mineral oil. A total of 192 20-cm photomultiplier tubes (PMTs) are radially positioned in the mineral-oil region of each AD. Further details on the AD, including details of calibration and vertex reconstruction, can be found in Ref. [20, 22]. The muon system design and performance are described in detail in Ref. [21].

3 Muon Data

3.1 Muon Event Selection Criteria

A muon candidate is defined as an event where (I) the reconstructed energy in an AD is larger than 60 MeV, and (II) more than 12 photomultipliers in the muon system (either IWS or OWS) produce a trigger within a 2 µs time window. We refer to (II) as the muon tag. The reconstructed energy spectrum of events with energy greater than 10 MeV is shown in Fig. 2, where the orange histogram represents all AD events with energy larger than 10 MeV, and the blue histogram represents the muon system tagged candidates. The difference between the two distributions is highlighted in green, and shows that untagged events with more than 20 MeV reconstructed energy experience a cut-off at roughly half the mass of a muon, typical of electrons originating from stopping muon decay. Such events are cleanly rejected by our selection criteria.

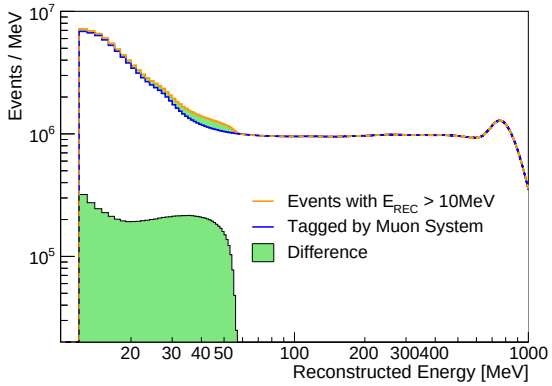

Figure 2. Reconstructed energy spectrum of muon candidate events in EH1 AD1 with and without the muon tag.

An important requirement for the selection criteria is to be stable over time, which in turn ensures the stability of the muon tagging procedure. The stability of the muon system is described in [21]. The stability of the energy scale for events taking place in both the GdLS and LS regions is guaranteed by weekly calibration campaigns [22] that provide the calibration constants used in the standard IBD analysis. However, the stability of the events taking place in the external buffer cannot be easily assessed. This region is filled with mineral oil (MO), and it was designed to shield the target volume from external radioactivity, hence it lacks any calibration system. Neutrino interactions taking place in the buffer result in no scintillation light, but muons passing through this region emit Cherenkov light, potentially resulting in events that are uncalibrated and should be vetoed. The left panel of Fig. 3 shows the event vertex distribution as a function of the energy cut for energy depositions taking place in EH1 AD1. Events whose vertex is reconstructed in the MO buffer ($R > 2$ m) clearly cluster at low energy, and are efficiently rejected by a 60 MeV cut. To further enhance the stability over time of the muon selection criteria, we correct for the permille-level energy drifts that the ADs experience because of the liquid scintillator aging. Such corrections are derived from fits to the ^{208}Tl spectrum due to residual radioactivity in the scintillator.

The only exception to the selection criteria introduced so far is EH3 AD1. We know that in this AD a tiny leak of liquid scintillator from the LS region to the buffer started in

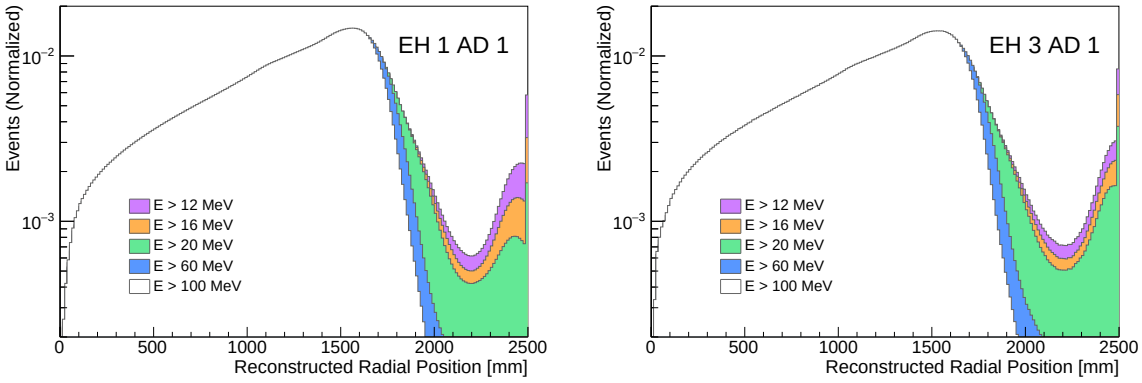

Figure 3. Comparison of the reconstructed radial distribution of muon candidate events in EH1 AD1 (left) and EH3 AD1 (right). In the analysis, the MO region is treated as a single bin [2000 mm, 2500 mm]; here we provide finer binning for comparison only.

Summer 2012. The LS and MO levels stabilized in 2014 when an estimated 50 L of LS had leaked into the MO [23]. As a consequence, the MO light yield increased, and the 60 MeV energy cut was more likely to select muons crossing the buffer region. To account for such a difference in light yield, we raise the energy cut of EH3 AD1 to 100 MeV, and we consider this AD separately from the others when computing systematic uncertainties.

3.2 Muon Rate Variation Over Time

Muon events are selected from a dataset collected between December 2011 and November 2013. The first 7 months of data taking are characterised by having only 6 operating ADs [24], while the last 13 months exploit the full 8-AD configuration.

The daily muon rate as a function of time in all the ADs is shown in Fig. 4. A fit with a sinusoidal function is performed to each AD separately, with the aim of checking if the modulation features are compatible among ADs. Fit parameters are reported in Table 2. The oscillation period is compatible with one solar year, and the position of the oscillation maximum (i.e. the oscillation phase) occurs consistently towards the end of July. The oscillation amplitude depends on the average muon energy, and therefore on the overburden. The average rate of EH3 AD1 is lower than the other ADs in the same experimental hall because of the tighter energy cut.

We stress that the sinusoidal fit is not used in the correlation analysis, but merely to enable a comparison among ADs as described above. The inability of a simple sinusoid to describe features such as the jump in the muon rate around March 2013 should not be considered a limitation. Indeed, the daily correlation of muon data with atmospheric temperature data is able to correctly account for such deviations from the sinusoidal function.

3.3 Muon Threshold Energy

The intensity of the cosmic muon flux I_μ is known to be dependent on the muon energy E_μ [25]. In the case of underground experiments, the muon energy spectrum is truncated, because low-energy muons get stopped by the rock above each experimental site. Here we define "threshold energy" ($E_{\rm thr}$) to be the minimum energy that a muon must have at the

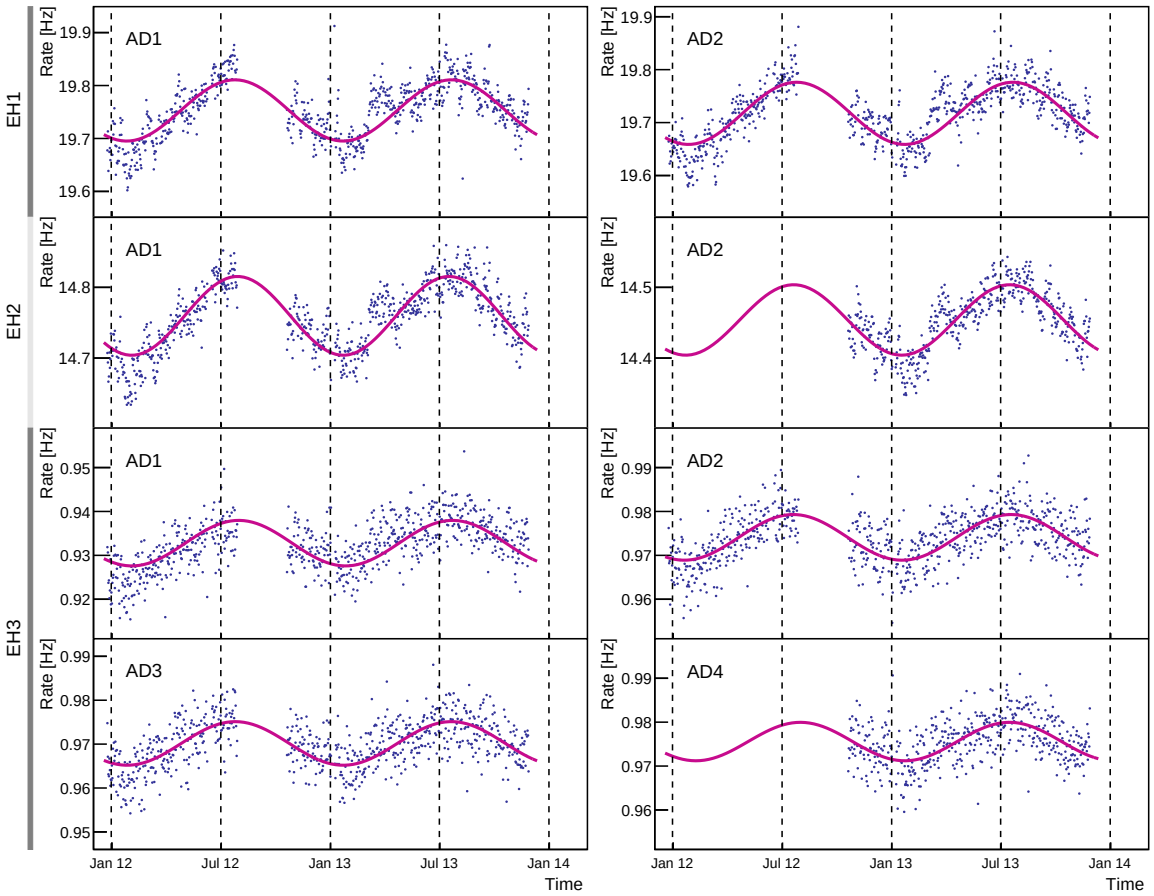

Figure 4. Daily-binned muon rate as function of time in the eight ADs. The solid line shows the result of a sinusoidal fit to data. Fit parameters are shown in Table 2.

Detector		Maximum	Period
EH1	AD1	21 Jul $\pm$ 2 days	361 $\pm$ 1 day
	AD2	21 Jul $\pm$ 2 days	361 $\pm$ 1 day
EH2	AD1	17 Jul $\pm$ 2 days	353 $\pm$ 1 day
	AD2	15 Jul $\pm$ 4 days	360 $\pm$ 3 days
EH3	AD1	22 Jul $\pm$ 4 days	356 $\pm$ 3 days
	AD2	18 Jul $\pm$ 5 days	363 $\pm$ 4 days
	AD3	20 Jul $\pm$ 5 days	360 $\pm$ 4 days
	AD4	15 Jul $\pm$ 10 days	348 $\pm$ 8 days

Table 2. Parameters resulting from fitting the muon modulation with a sinusoidal function.

surface in order to reach an experimental hall. Liquid scintillator experiments are in general not able to measure E_μ, hence the muon rate they measure is the integral of $I_\mu(E_\mu)$ from $E_{\rm thr}$ to the maximum cosmic muon energy. As a consequence, $E_{\rm thr}$ is one of the most important parameters differentiating experiments that perform inclusive measurements of the muon flux

at different underground depths. In this analysis, E_{thr} plays two roles: first, it is involved in the procedure to compute the effective atmospheric temperature T_{eff} (Eq. 4.2), and second, it allows us to compare the measured muon modulation against both an atmospheric model (Eq. 6.1) and other experiments (Fig. 9).

To determine E_{thr} at the three Daya Bay experimental sites we rely on MC simulations. Namely, we simulate cosmic muon propagation through the overburden using the topographic maps of the three experimental sites (see Fig. 1) with the MUSIC simulation package [26]. The overburden is assumed to be made of standard rock, defined to have atomic number 11, atomic mass 22, and density $2.65\,\text{g/cm}^3$. We generate more than 1 million muons at the surface of each site according to the modified Gaisser formula [27], where the exact number is chosen such that 10^5 muons reach the experimental hall. For each muon, we record its zenith angle θ, its azimuthal angle ϕ and its energy, both at the surface (before propagation) and at experimental hall (after propagation), which results in a site-dependent $E_\mu(\theta, \phi)$ distribution. In the theoretical model describing the seasonal modulation of the muon flux, E_{thr} always appears multiplied by the cosine of the zenith angle (evaluated at the surface), resulting in the expression $E_{\text{thr}} \cos\theta$. We therefore marginalise the azimuthal dependency, $E_\mu(\theta) = \int \mathrm{d}\phi\, E_\mu(\theta, \phi)$, and bin the resulting energy distribution in terms of $\cos\theta$. Each angular bin is then characterised by an energy spectrum, whose starting point we define to be E_{thr}. This procedure results in a $\cos\theta$- and site-dependent E_{thr}, which is shown in the right panel of Fig. 5.

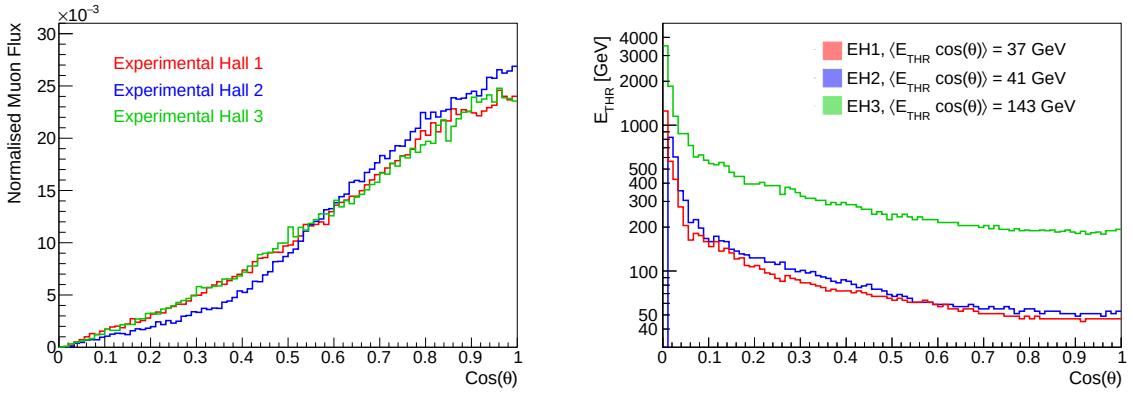

Figure 5. (Left) Underground muon flux normalised to unity as a function of the cosine of the zenith angle $\cos\theta$ at the surface. (Right) Minimum or threshold energy needed for a muon to reach an experimental hall E_{thr} as a function of $\cos\theta$. Small-scale structures are ascribable to statistical fluctuations of the MC simulation and not to a rapidly changing mountain profile.

The zenith angle dependency of the term $E_{\text{thr}} \cos\theta$ results from two competing effects: (I) cosmic ray primaries coming from the horizon interact higher in the atmosphere, enhancing the probability of secondary mesons to decay into muons, and (II) a lower fraction of such cosmic muons reach the detector because the overburden increases rapidly towards the horizon. In principle, the former considerations could be exploited to investigate how the muon rate modulation changes as a function of the zenith angle [15]. However, pointing information is not currently extracted in our reconstruction, so this analysis considers only inclusive quantities. For this reason, we average $E_{\text{thr}} \cos\theta$ over all the zenith angles:

$$\langle E_{\text{thr}} \cos\theta \rangle = \sum_i E_{\text{thr}}(c_i) \cdot n(c_i) \cdot c_i \tag{3.1}$$

where the index i runs over the bins of the histograms shown in Fig. 5, c_i is the value of $\cos\theta$ at the bin center, and $n(c_i)$ is the muon flux normalized to unity evaluated at the i-th angular bin, as shown in the left panel of Fig. 5. The $\langle E_{\rm thr}\cos\theta\rangle$ values for EH1, EH2 and EH3 are 37 GeV, 41 GeV and 143 GeV, respectively.

The systematic uncertainty on $\langle E_{\rm thr}\cos\theta\rangle$ breaks down into three major components: (I) angular resolution, (II) energy resolution, and (III) imperfect knowledge of the topographic map. We quantify (I) as the bin width chosen for the $\cos\theta$ distribution, which results in a 1.1% relative uncertainty, and (II) as the bin width of the $E_{\rm thr}$ spectrum, which results in a $2\,{\rm GeV}/E_{\rm thr}$ relative uncertainty. Component (III) is evaluated by shifting the mountain elevation profile up and down by 6 m, which is the altitude resolution of the topographic map. This procedure yields a 6% relative uncertainty. It is worth stressing that both an increase in the elevation profile and an increase in the rock density result in a larger $E_{\rm thr}$, since both contribute to enhance the mountain stopping power. As a consequence, (III) also accounts for the difference between standard rock and the actual Daya Bay rock. The overall relative systematic uncertainty on $\langle E_{\rm thr}\cos\theta\rangle$ is assessed by summing the squared values (I), (II) and (III), which gives an overall 7% systematic uncertainty.

4 Temperature Data

4.1 Effective Atmospheric Temperature

The atmospheric temperature data at the Daya Bay site was obtained from the ERA-Interim database supplied by the European Centre for Medium-Range Weather Forecasts (ECMWF) [28]. The database comprises different types of measurements (ground level, sounding balloon, satellite) at many locations over the world, and exploits a global atmospheric model to interpolate to a particular location [29]. Our analysis relies on the temperature values computed at the Daya Bay site (22.6°N, 114.5°E), which are provided four times a day (midnight, 6am, noon, 6pm) at 37 discrete pressure levels ranging from 1 hPa to 1000 hPa. The interpolated temperature dataset has a spatial resolution of $0.25^\circ \times 0.25^\circ$, hence all the three Daya Bay experimental halls share the same raw temperature dataset.

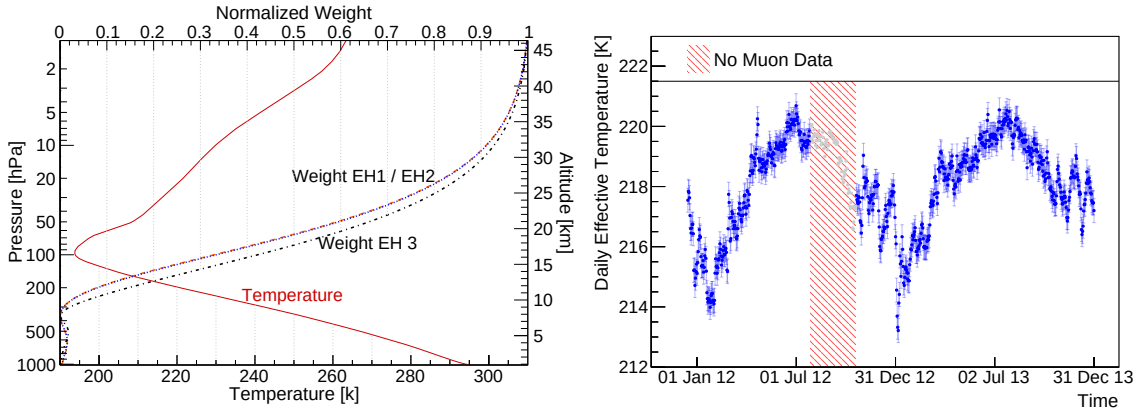

Figure 6. (Left) EH-dependent weights involved in the $T_{\rm eff}$ computation and time-averaged atmospheric temperature, both as a function of pressure and altitude. (Right) Daily $T_{\rm eff}$ values computed using EH1 weights. "No Muon Data" refers to the 2012 summer shutdown.

Our goal is to use the atmospheric temperature to assess if and how it affects the muon production. However, it is not possible to know at what altitude a cosmic muon is produced, hence we follow [1, 11, 30] and approximate the atmosphere with an isothermal body characterised by an effective temperature T_{eff}. T_{eff} is defined as the temperature that would cause the observed muon intensity if the atmosphere were isothermal [1], and it is computed as a weighted average of the temperature T over the atmospheric depth X, with weights W, as shown in Eq. 4.1.

$$T_{\text{eff}} = \frac{\int_0^\infty \mathrm{d}X\, T(X)\, W(X)}{\int_0^\infty \mathrm{d}X\, W(X)} \simeq \frac{\sum_i \Delta X_i\, T(X_i)\, W(X_i)}{\sum_i \Delta X_i\, W(X_i)} \tag{4.1}$$

The atmospheric depth X is expressed in g/cm^2 and is related to the pressure level by the relation 1 hPa = 1.019 g/cm^2. The approximation with the discrete summation is appropriate because the temperature data is available only at discrete pressure levels.

The weight W associated with each pressure level reflects the model that we use to explain the modulation of the muon flux (see below). The left panel of Fig. 6 shows that pressure levels near the top of the atmosphere are weighted more heavily than the pressure levels at lower altitude. The two main arguments to support this choice are: (I) a high energy parent meson has less chance to decay after it reaches the high density regions at low altitude, and (II) very few of the parent mesons survive both nuclear interaction and decay long enough to reach low altitude.

Both kaon and pion production and decay should be considered in the model [1]. However, because of limited sensitivity to the kaon contribution, older experiments computed their weights using a pion-only model (e.g. Barrett [1], Sherman [3], Utah [17], MACRO [11]). This approach changed with MINOS [16] which, for the first time, used a model put forward by Grashorn et al. [30] explicitly including kaons. Here we follow the latter approach, and we write $W(X_i) = W^\pi(X_i) + W^K(X_i)$, where

$$W^{\pi,K}(X) \simeq \frac{\left(1 - \frac{X}{\lambda_{\pi,K}}\right)^2 e^{-\frac{X}{\Lambda_{\pi,K}}}\, A_{\pi,K}}{\gamma + (\gamma+1) B_{\pi,K}\, K(X) \left(\frac{\langle E_{\text{thr}} \cos\theta\rangle}{\epsilon_{\pi,K}}\right)^2} \tag{4.2a}$$

$$K(X) \equiv \frac{X\, \left(1 - \frac{X}{\lambda_{\pi,K}}\right)^2}{\left(1 - e^{-\frac{X}{\lambda_{\pi,K}}}\right) \lambda_{\pi,K}} \tag{4.2b}$$

$$\frac{1}{\lambda_{\pi,K}} = \frac{1}{\Lambda_N} - \frac{1}{\Lambda_{\pi,K}}\ . \tag{4.2c}$$

$A_{\pi,K}$ is a constant comprising the amount of inclusive meson production in the forward fragmentation region, the masses of mesons and muons, and the muon spectral index. The parameter $B_{\pi,K}$ accounts for the relative atmospheric attenuation of mesons. The parameter $\Lambda_{N,\pi,K}$ is the atmospheric attenuation length of the cosmic ray primaries, pions and kaons, respectively. The meson critical energy, $\epsilon_{\pi,K}$, is the meson energy for which decay and interaction have an equal probability. Finally, the parameter γ is the muon spectral index.

The values of all the parameters are listed in Table 3 and are inherited from [16], with the exception of $\langle E_{\text{thr}} \cos\theta\rangle$ calculated as described. The left panel of Fig. 6 shows three

Parameter	Value	Reference
A_π	1	[16]
A_K	$0.38 \cdot r_{K/\pi}$	[16]
$r_{K/\pi}$	0.149 ± 0.06	[32]† , [33]‡
B_π	1.460 ± 0.007	[16]
B_K	1.740 ± 0.028	[16]
Λ_N	120 g/cm^2	[32]
Λ_π	180 g/cm^2	[32]
Λ_K	160 g/cm^2	[32]
$\langle E_{\rm thr} \cos\theta \rangle_{\rm EH1}$	37 ± 3 GeV	
$\langle E_{\rm thr} \cos\theta \rangle_{\rm EH2}$	41 ± 3 GeV	
$\langle E_{\rm thr} \cos\theta \rangle_{\rm EH3}$	143 ± 10 GeV	
γ	1.7 ± 0.1	[34]
ϵ_π	114 ± 3 GeV	[16]
ϵ_K	851 ± 14 GeV	[16]

Table 3. Central values and uncertainties of the parameters used in Eq. 4.2. † Reference for the central value. ‡ Reference for the uncertainty.

weight functions —due to the fact that the $E_{\rm thr}$ value is site dependent— together with the time-averaged temperature at the Daya Bay site. The $T_{\rm eff}$ daily values computed at EH1 are shown in right panel of Fig. 6.

4.2 Temperature Uncertainty

To assess the uncertainty on the daily effective temperature $\sigma(T_{\rm eff})$, we compute $T_{\rm eff}$ again starting from a different temperature dataset, and we consider the spread of the difference between the new and old values to be a conservative estimate of the $T_{\rm eff}$ uncertainty. The new dataset is the Integrated Global Radiosonde Archive (IGRA) [31] provided by the US National Climatic Data Center. It comprises temperature data from sounding balloons launched from many meteorological stations around the world, where the closest station to our detectors is located in the city of Shantou, Guandong (China), 235 km North-East of Daya Bay. As mentioned in the previous section, the ECMWF dataset can be interpolated to an arbitrary location, hence –for the sake of this comparison– we compute an ECMWF-based $T_{\rm eff}$ at the Shantou's coordinates (23°21′N, 116°40′E), and we compare it with the IGRA-based $T_{\rm eff}$. The distribution of the differences shows a spread of 0.4 K, which we propagate to the $T_{\rm eff}$ uncertainty. As a further check, we also compare ECMWF-based $T_{\rm eff}$ values computed at Daya Bay's coordinates with IGRA-based $T_{\rm eff}$ values computed at Shantou, and we find the spread to be the same.

The uncertainties associated with all the parameters involved in Eq. 4.2 also contribute an additional temperature systematic uncertainty. To evaluate the impact, we proceed as follows: (I) we associate to each parameter a Gaussian distributed independent random variable, where the mean value and the sigma are chosen according to the values in Table 3, (II) we generate 10^5 weight functions (like those shown in Fig. 6) using a random point in the parameter phase-space, (III) with each generated weight function we carry out a new $T_{\rm eff}$ calculation, resulting in 10^5 smeared $T_{\rm eff}$ values per day. We build a daily distribution of the difference between the smeared and the nominal $T_{\rm eff}$ values, and we find that over the whole data-taking period the spread induced by smearing the weights is 0.15 K, 0.15 K,

0.07 K, respectively for EH1, EH3 and EH3. Combining these uncertainties with the 0.4 K T_{eff} uncertainty common to all the experimental halls, we get a total $\sigma(T_{\text{eff}})$ of 0.43 K, 0.43 K and 0.41 K respectively.

5 Correlation Analysis

The aim of this analysis is to assess quantitatively how a variation in the atmospheric temperature relates to a variation in the underground muon rate. For each AD we start from a daily binned T_{eff} dataset (common to all the ADs within an experimental hall) and from a daily binned muon rate dataset, and we build a scatter plot where the x (y) axis represents the temperature (muon rate) relative variation with respect to its mean value. All the scatter plots are shown in Fig. 7. The y error bar on each data point represents the Poissonian uncertainty on the number of detected muons, while the x error bar represents the temperature uncertainty obtained by comparing two temperature datasets (see previous section).

A linear regression accounting for errors on both axes is performed to each scatter plot. We use the fitting routines provided by ROOT [35], and we define the slope of the fitted linear function to be the correlation coefficient α. As a crosscheck, the same regression is performed using a *Numerical Recipes'* algorithm [36], yielding identical results.

5.1 Systematics Study

Systematic uncertainties affecting the correlation coefficients can be divided into regression-related and muon-related. The former deal with the absence of two complete oscillation cycles in the muon data. No AD continuously acquires data for more than one period due to the Summer 2012 shutdown and the lack of the first seven months of data for the two ADs. To check the impact of computing the correlation coefficient on a limited time range, we use EH1 AD1, EH1 AD2 and EH2 AD1 data, since these ADs have reduced statistical uncertainties (muon rates are higher because the experimental sites are shallower), and they collected data both before and after the shutdown. Using these ADs, we compute two separate correlation coefficients for the pre- and post-shutdown periods, and we find a maximum discrepancy of 8%, which we take to be the systematic uncertainty associated with the fitting range.

We define muon-related systematics to be those uncertainties that are expected not only to inflate the correlation coefficient uncertainty, but also to bias its central value (as opposed to the statistical uncertainties that are already included in the linear regression). For this reason, muon-related systematics are evaluated by performing new linear regressions with slightly different muon datasets. The two effects we want to study are the AD-dependent correction of the energy drift over time, and the tighter energy cut for EH3 AD1, resulting from the liquid scintillator leakage into the MO region. All the energy drift corrections are below 1%. As a consequence, we conservatively shift the energy thresholds used in the muon selection criteria up and down by 1%, and we perform new linear regressions based on the higher/lower energy datasets. The corresponding correlation coefficients deviate at most 3% from the nominal values, hence we assign a 3% systematic uncertainty to all the ADs. The effect of the tighter energy cut on EH3 AD1 is two-fold. (i) Daya Bay electronics distinguishes two energy ranges, "fine" and "coarse", depending on the PMT output charge.

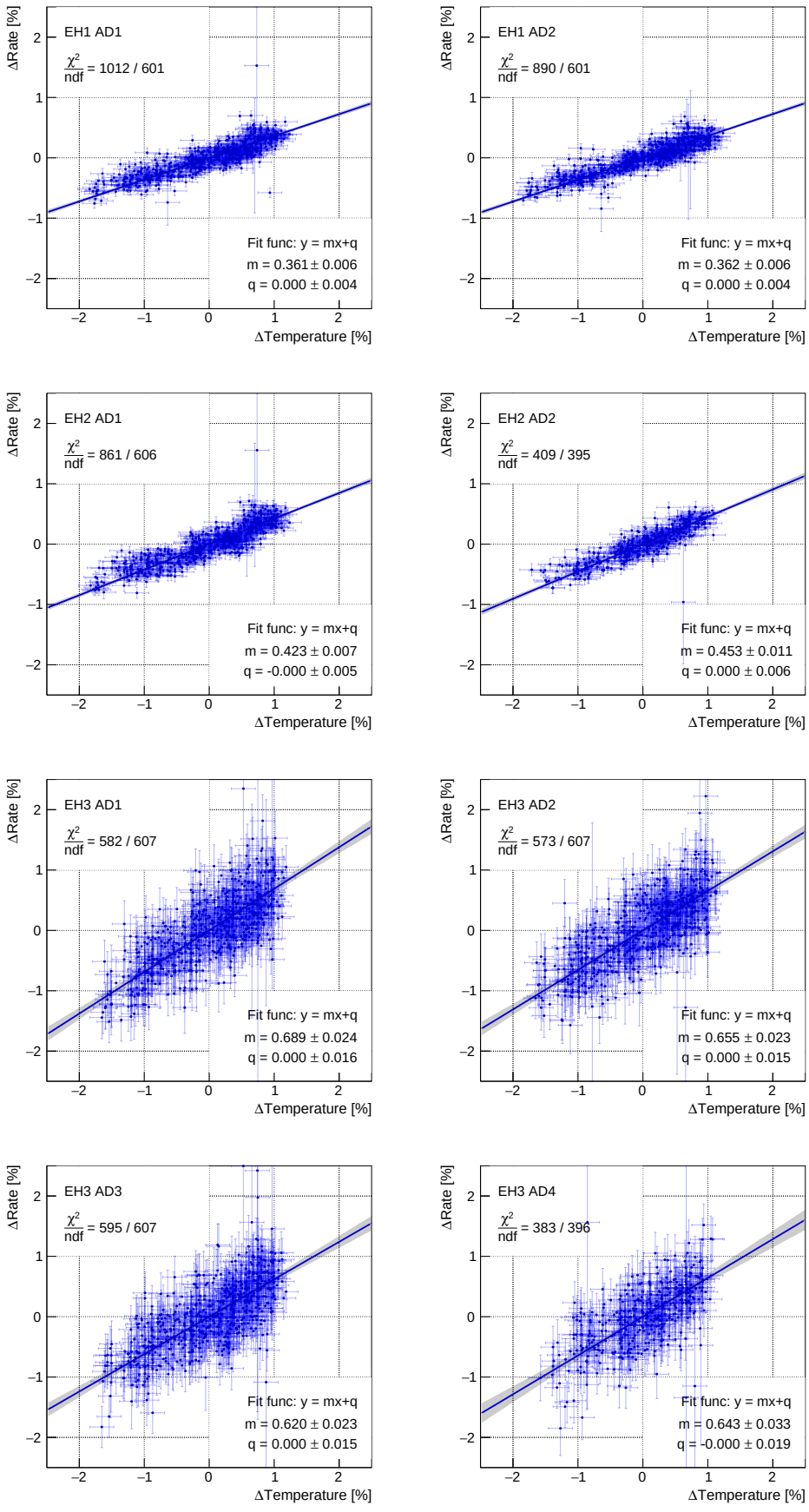

Figure 7. Relative muon rate variation vs relative effective temperature variation as measured in the eight ADs, together with the result of a linear regression accounting for uncertainties on both variables.

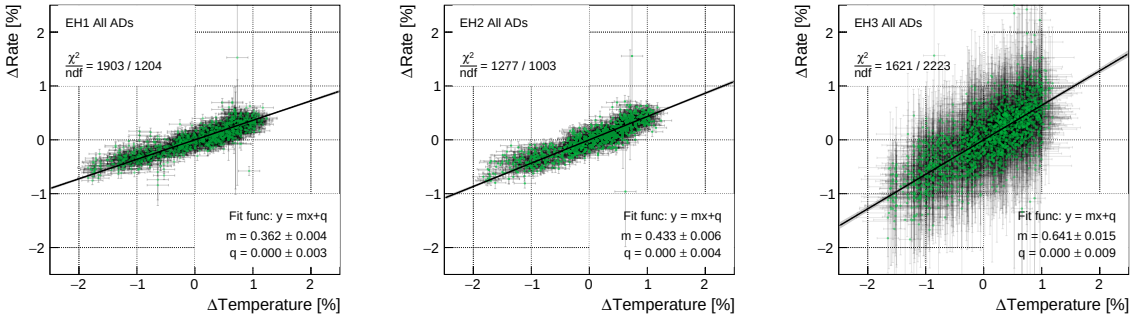

Figure 8. Relative muon rate variation vs relative effective temperature variation constructed by merging data from ADs belonging to the same experimental hall, together with the result of a linear regression accounting for uncertainties on both variables

The "fine" (lower) range is well calibrated since it is used for precision neutrino physics, while the higher range is meant only to tag cosmic muons and is less precisely calibrated. The event-level energy threshold of 100 MeV therefore results in some of the channels operating in the "coarse" energy range, whose stability over time is more uncertain. To assess the impact of these effects we raise the energy cut from 60 MeV to 100 MeV in the EH1 and EH2 ADs, and we look at variation in the α values. The reason for considering EH1 and EH2 is to exploit their larger muon flux and to avoid that a shift in α might be ascribed to statistical fluctuations. This test results in a 2% variation of the α value. (II) The tighter energy cut might not efficiently reject all the muons passing through the MO region, hence there might be a bias introduced by this residual contamination. To assess its relevance, we compare the number of events with $R > 2$ m across all the EH3 ADs, and we see that, despite a higher energy cut, EH3 AD1 collects more events. Moreover, the event excess is confined to post-Summer 2012, increasing our confidence in ascribing those events to the LS leak. We further evaluate the outcome of such contamination on the correlation coefficient by performing the EH3 AD1 regression on a new muon dataset comprising an additional $R < 2$ m vertex cut. We find the difference between the new and the nominal correlation coefficient to be at the level of 4%. The total systematic uncertainty affecting EH3 AD1 is therefore 5.4%.

Results are summarised in Table 4.

5.2 Correlation Coefficient Combination

The correlation coefficient between the muon rate variation and the atmospheric temperature variation is known to increase as a function of the overburden, as a result of a harder muon energy spectrum. For this reason we combine the results obtained from ADs sharing the same experimental hall, with the aim to provide our results as a function of $\langle E_{\rm thr} \cos\theta \rangle$. Coefficient uncertainties in the same experimental hall are partially correlated, since they share the same temperature dataset. Instead of combining the values, we choose to merge the raw datasets and to perform a new linear regression on the combined scatter plots, as shown in Fig. 8. This procedure has also the advantage that no fit relies on a truncated dataset — such as EH2 AD2, and EH3 AD4.

Systematic uncertainties common to all the ADs can directly be applied to the combined correlation coefficients. However special care must be devoted to handling EH3 AD1. Indeed this AD has its own systematic uncertainty resulting from the LS leak, and must be weighted

Detector		Correlation Coefficient	Uncertainty Stat.	Sys.	Tot.	Combined
EH1	AD1	0.3614	0.0062	0.0309	0.0315	0.362 ± 0.031
	AD2	0.3624	0.0062	0.0310	0.0316	
EH2	AD1	0.4232	0.0071	0.0362	0.0369	0.433 ± 0.038
	AD2	0.4530	0.0107	0.0387	0.0402	
EH3	AD1	0.6890	0.0240	0.0664	0.0707	0.641 ± 0.057
	AD2	0.6549	0.0234	0.0560	0.0607	
	AD3	0.6200	0.0234	0.0530	0.0579	
	AD4	0.6427	0.0334	0.0549	0.0643	

Table 4. Experimental values of the correlation coefficient (α) per detector.

accordingly in the EH3 combination. To this end we exploit a feature of the linear regression, namely the fact that applying a scale factor to the error bars of the data points being fitted, results in a proportional scaling of the fit uncertainty. We therefore scale the error bars of the EH3 AD1 data points by the amount $\sigma_{\text{tot}}/\sigma_{\text{stat}}$, where $\sigma_{\text{tot}} = \sqrt{\sigma_{\text{stat}}^2 + \sigma_{\text{sys}}^2}$. In this way, fitting the EH3 AD1 dataset with inflated uncertainties results in a fit uncertainty which includes the systematic one. As a result, the EH3 AD1 data points are now correctly weighted in the combined EH3 fit. The correlation coefficients of the three experimental halls are summarised in Table 4.

6 Comparison With Model Prediction and Other Experiments

The model prediction for α can be written as:

$$\alpha = \frac{T_{\text{eff}}}{I_\mu} \frac{\partial I_\mu}{\partial T_{\text{eff}}} \,. \tag{6.1}$$

Grashorn et al. [30] show that this prediction can be expressed in terms of both pion and kaon contributions as

$$\alpha = \frac{1}{D_\pi} \frac{1/\epsilon_K + A_K (D_\pi/D_K)^2/\epsilon_\pi}{1/\epsilon_K + A_K (D_\pi/D_K)/\epsilon_\pi} \,, \tag{6.2}$$

where

$$D_{\pi,K} = \frac{\gamma}{\gamma+1} \frac{\epsilon_{\pi,K}}{1.1 \, \langle E_{\text{thr}} \cos\theta \rangle} + 1 \,. \tag{6.3}$$

Equation 6.2 can be reduced to MACRO's previously published α [11], which is only valid for pion-induced muons, by setting $A_K = 0$ (i.e. no kaon contribution). To get the model prediction of α for the three Daya Bay sites, we plug the parameter values listed in Table 3 into Eq. 6.2. We consider both the model accounting for π and K and the model accounting for π only, and we report our findings in Table 5. The two models are shown in Fig. 9.

To quantify the systematic uncertainty associated with the model prediction, we smear each input parameter according to its uncertainty, and in Table 6 we assess its impact on the α prediction. As expected, the $\langle E_{\text{thr}} \cos\theta \rangle$ uncertainty is driving the overall error budget. By comparing the experimental with the predicted α values (Table 5), it can be noticed that the former are consistently larger than the latter, hence favoring a lower kaon contribution with respect to the one currently used in literature ($r_{K/\pi} = 0.149$ [12, 15, 16, 32]).

Exp. Hall	Prediction		This Work
	Including K and π [30]	Including π only [11]	
EH1	0.340 ± 0.019	0.362 ± 0.018	0.362 ± 0.031
EH2	0.362 ± 0.019	0.386 ± 0.018	0.433 ± 0.038
EH3	0.630 ± 0.019	0.687 ± 0.018	0.641 ± 0.057

Table 5. Predicted and measured values of the correlation coefficient at the different experimental halls.

Systematic Uncertainty		Resulting
Parameter	Magnitude	Uncertainty on α
$\langle E_{\rm thr} \cos\theta \rangle$	7.0%	0.015
$R_{K/\pi}$	4.0%	0.0085
ϵ_π	2.6%	0.0055
ϵ_K	1.6%	0.000 11
γ	5.9%	0.0049
Total		0.019

Table 6. Systematic uncertainties affecting the theoretical prediction of the correlation coefficient.

Figure 9 shows how the Daya Bay result compares to other experiments[1] and to the model prediction. All the correlation coefficients are presented as a function of $\langle E_{\rm thr} \cos\theta \rangle$, since this is the only free parameter in Eq. 6.3. We stress here that such a quantity is sensitive not only to the vertical depth, but also to the shape of the overburden. Indeed, the muon energy loss is determined by the amount of material crossed. In the case of a flat overburden, however, $\langle E_{\rm thr} \cos\theta \rangle$ can be well approximated with the minimum value of $E_{\rm thr}$, namely the value evaluated along the vertical direction $E_{\rm thr}(\theta = 0)$. For this reason many experiments quote only the $E_{\rm thr}$ quantity. To assess to what extent this approximation holds, we use a toy Monte Carlo to scan the quantity $\langle E_{\rm thr}(\theta) \cos\theta \rangle / E_{\rm thr}(0)$ at various depths, and we find that the deviation grows monotonically with the overburden, and stays below 10% up to 1.6 kmwe. For experiments not quoting any uncertainty on $E_{\rm thr}$, we use this deviation to associate a horizontal error bar to the points shown in Fig. 9. Two exceptions are the Baksan and Gran Sasso experiments. The Baksan overburden is non-flat, and the average cosmic muon zenith angle is $\langle\theta\rangle = 35^\circ$ [37]. We consider $E_{\rm thr} \cos\langle\theta\rangle$ to be a lower bound to $\langle E_{\rm thr} \cos\theta \rangle$, hence we use the Baksan's quoted $E_{\rm thr}$ as the central value, and the difference between $E_{\rm thr}$ and $E_{\rm thr} \cos\langle\theta\rangle$ as the uncertainty. The MACRO collaboration measured the minimum $E_{\rm thr}$ at the Gran Sasso laboratory to be 1300 GeV. From their α prediction based on a Monte Carlo simulation accounting for the Gran Sasso mountain profile, it can be inferred that $\langle E_{\rm thr} \cos\theta \rangle \sim 1600$ GeV. For all Gran Sasso experiments we take the latter as central value, and the difference with respect to $E_{\rm thr}$ as uncertainty. Such an uncertainty is large enough to accomodate Borexino's and Gerda's $E_{\rm thr}$ values, which are based on Grashorn's flat approximation [30].

[1] Experiments such as Torino [4], Hobart [5], Poatina [7, 8], and Matsushiro [6] are not included in this comparison, because they perform a combined regression trying to correlate their muon rate with the pressure measured at sea level (barometric coefficient) and the atmospheric temperature (temperature coefficient) at the same time. Such measurements cannot be easily compared in a plot with all the others, which are based only on the correlation between muon rate and atmospheric temperature.

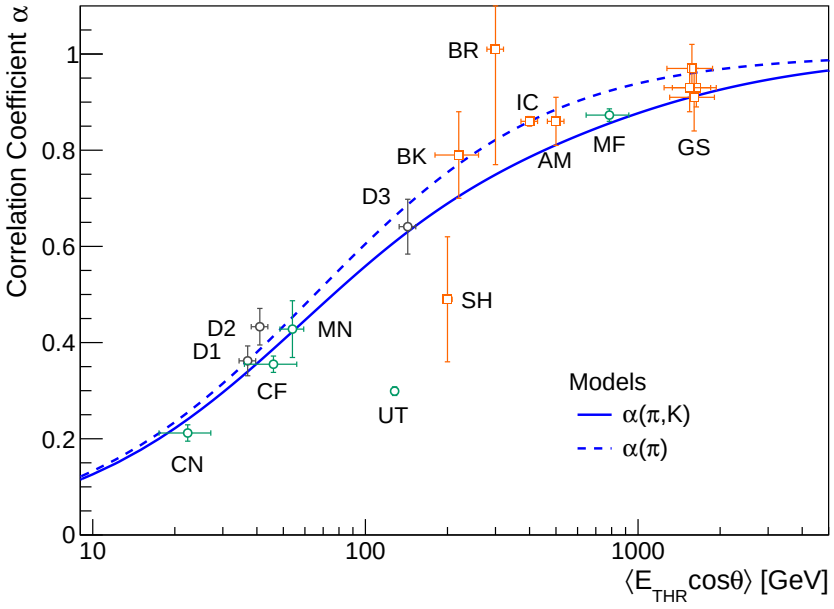

Figure 9. Comparison of the experimental α values with the model accounting for pions and kaons (solid line), and with the model accounting for pions only (dashed line). Values determined in this analysis are reported as D1, D2 and D3 respectively for the three experimental halls. Other experiments include Amanda (AM) [10], Baksan (BK) [9], Barrett (BR) [2], Icecube (IC) [14], MINOS Near (MN) [15] and far (MF) [16] detector, Double Chooz Near (CN) and Far (CF) detectors [19], Sherman (SH) [3], and Utah (UT) [17]. The four Gran Sasso (GS) based measurements are MACRO [11], Borexino [12], and the two Gerda values [18]. Their $\langle E_{\rm thr}\cos\theta\rangle$ are artifically displaced on the horizontal axis for the sake of visualization. The values and uncertainties of $\langle E_{\rm thr}\cos\theta\rangle$ shown in the Figure for experiments tagged with a square marker have been estimated as described in the text.

7 Conclusion

Muon rate variations over a time period of two years were measured using all the active components of the Daya Bay experiment. Muon rates were then correlated with the effective atmospheric temperature above the three experimental halls. The effective temperature is the result of a weighted average over all the pressure levels comprised in the raw temperature dataset provided by the European Centre for Medium-Range Weather Forecasts, and is needed to account for the fact that the majority of the muons are produced in the uppermost layers of the atmosphere. The correlation coefficient α at the three experimental halls was found to be:

$$\begin{aligned}
\alpha_{\rm EH1} &= 0.362 \pm 0.031 \quad \text{at} \quad \langle E_{\rm thr}\cos\theta\rangle_{\rm EH1} = 37 \pm 3 \text{ GeV} \\
\alpha_{\rm EH2} &= 0.433 \pm 0.038 \quad \text{at} \quad \langle E_{\rm thr}\cos\theta\rangle_{\rm EH2} = 41 \pm 3 \text{ GeV} \\
\alpha_{\rm EH3} &= 0.641 \pm 0.057 \quad \text{at} \quad \langle E_{\rm thr}\cos\theta\rangle_{\rm EH3} = 143 \pm 10 \text{ GeV}
\end{aligned}$$

The importance of this measurement lies in the fact that Daya Bay is the only experiment so far able to probe the muon seasonal variation at different overburdens using identically designed detectors. Moreover, data from the three EHs represent an important validation of the model, since the Daya Bay data point happens to be in a region where α strongly depends on $\langle E_{\rm thr}\cos\theta\rangle$.

Acknowledgments

Daya Bay is supported in part by the Ministry of Science and Technology of China, the U.S. Department of Energy, the Chinese Academy of Sciences, the CAS Center for Excellence in Particle Physics, the National Natural Science Foundation of China, the Guangdong provincial government, the Shenzhen municipal government, the China Guangdong Nuclear Power Group, Key Laboratory of Particle and Radiation Imaging (Tsinghua University), the Ministry of Education, Key Laboratory of Particle Physics and Particle Irradiation (Shandong University), the Ministry of Education, Shanghai Laboratory for Particle Physics and Cosmology, the Research Grants Council of the Hong Kong Special Administrative Region of China, the University Development Fund of The University of Hong Kong, the MOE program for Research of Excellence at National Taiwan University, National Chiao-Tung University, and NSC fund support from Taiwan, the U.S. National Science Foundation, the Alfred P. Sloan Foundation, the Ministry of Education, Youth, and Sports of the Czech Republic, the Joint Institute of Nuclear Research in Dubna, Russia, the CNFC-RFBR joint research program, the National Commission of Scientific and Technological Research of Chile, and the Tsinghua University Initiative Scientific Research Program. We acknowledge Yellow River Engineering Consulting Co., Ltd., and China Railway 15th Bureau Group Co., Ltd., for building the underground laboratory. We are grateful for the ongoing cooperation from the China General Nuclear Power Group and China Light and Power Company.

References

[1] P.H. Barrett *et al.* "Interpretation of Cosmic-Ray Measurements Far Underground", Rev. Mod. Phys. 24, 133 (1952).

[2] P.H. Barrett *et al.* "Atmospheric Temperature Effect for Mesons Far Undergound", Rev. Mod. Phys. 95, 1573 (1954).

[3] N. Sherman, "Atmospheric Temperature Effect for μ Mesons Observed at a Depth of 846 m.w.e.", Phys. Rev. **93**, 208 (1954), http://link.aps.org/doi/10.1103/PhysRev.93.208.

[4] G. Cini Castagnoli *et al.* "Trains of diurnal waves in the muonic component at 70 mwe during cosmic-ray decreases", J. Geophys. Res. 74, 2414 (1969), http://dx.doi.org/10.1029/JA074i009p02414.

[5] A. Fenton *et al.* "Cosmic ray observations at 42 mwe underground at Hobart, Tasmania" Nuovo Cimento 22, 285 (1961), http://dx.doi.org/10.1007/BF02783019.

[6] S. Yasue *et al.* , "Observation of cosmic ray intensity variation with Matsushiro underground telescope" 17th International Cosmic Ray Conference Volume 4. p. 308-311 (1981), http://adsabs.harvard.edu/abs/1981ICRC....4..308Y.

[7] J.E. Humble *et al.*, "Variations in Atmospheric Coefficients for Underground Cosmic-Ray Detectors" 16th International Cosmic Ray Conference, Vol. 4. p.258 (1970), http://adsabs.harvard.edu/abs/1979ICRC....4..258H.

[8] P.R.A. Lyons *et al.*, "Further calculations of atmospheric coefficients for underground cosmic ray detectors", 17th International Cosmic Ray Conference, Volume 4. p. 300-303 (1981), http://adsabs.harvard.edu/abs/1981ICRC....4..300L.

[9] Y. Andreyev *et al.* (Baksan Collaboration), "Season Behaviour of the Amplitude of Daily Muon Intensity with Energy ≥ 220 GeV", in Proceedings of the 22th ICRC, 693 (1991), http://adsabs.harvard.edu/abs/1991ICRC....3..693A.

[10] A. Bouchta (AMANDA Collaboration), "Seasonal Variation of the muon flux seen by Amanda", in Proceedings of the 26th ICRC [2, 108 (1999)], http://adsabs.harvard.edu/abs/1999ICRC....2..108B.

[11] M. Ambrosio *et al.* [MACRO Collaboration], "Seasonal variations in the underground muon intensity as seen by MACRO", Astropart. Phys. **7**, 109 (1997).

[12] G. Bellini *et al.* [Borexino Collaboration], "Cosmic-muon flux and annual modulation in Borexino at 3800 m water-equivalent depth", JCAP **1205**, 015 (2012) [arXiv:1202.6403].

[13] M. Selvi (LVD Collaboration), in Proceedings of the 31st ICRC, Lodz, Poland, 2009.

[14] P. Desiati *et al.* [IceCube Collaboration], "Seasonal Variations of High Energy Cosmic Ray Muons Observed by the IceCube Observatory as a Probe of Kaon/Pion Ratio", Proceedings of the 32nd International Cosmic Ray Conference (ICRC 2011), http://dx.doi.org/10.7529/ICRC2011/V01/0662.

[15] P. Adamson *et al.*, "Observation of muon intensity variations by season with the MINOS Near Detector", Phys. Rev. D **90**, no. 1, 012010 (2014) [arXiv:1406.7019].

[16] P. Adamson *et al.* [MINOS Collaboration], "Observation of muon intensity variations by season with the MINOS far detector", Phys. Rev. D **81**, 012001 (2010) [arXiv:0909.4012].

[17] D.J. Cutler and D.E. Groom, in Proceedings of the 17th ICRC, 290 ,Paris (1981), "Meteorological effects in cosmic ray muon production", http://adsabs.harvard.edu/abs/1981ICRC....4..290C.

[18] M. Agostini *et al.* [GERDA Collaboration], "Flux Modulations seen by the Muon Veto of the GERDA Experiment", Astropart. Phys. **84** (2016) 29 [arXiv:1601.06007 [physics.ins-det]].

[19] T. Abrahao *et al.* [Double Chooz Collaboration], "Cosmic-muon characterization and annual modulation measurement with Double Chooz detectors", JCAP **1702** (2017) no.02, 017 [arXiv:1611.07845 [hep-ex]].

[20] F. P. An *et al.* [Daya Bay Collaboration], "A side-by-side comparison of Daya Bay antineutrino detectors", Nucl. Instrum. Meth. A **685**, 78 (2012) [arXiv:1202.6181].

[21] F. P. An *et al.* [Daya Bay Collaboration], "The muon system of the Daya Bay Reactor antineutrino experiment", Nucl. Inst. Meth. A **773**, 8 (2015) [arXiv:1407.0275].

[22] F. P. An *et al.* [Daya Bay Collaboration], "Measurement of electron antineutrino oscillation based on 1230 days of operation of the Daya Bay experiment", Phys. Rev. D **95** (2017) no.7, 072006 [arXiv:1610.04802 [hep-ex]].

[23] F. P. An *et al.* [Daya Bay Collaboration], "The Detector System of The Daya Bay Reactor Neutrino Experiment", Nucl. Instrum. Meth. A **811** (2016) 133 doi:10.1016/j.nima.2015.11.144 [arXiv:1508.03943 [physics.ins-det]].

[24] F. P. An *et al.* [Daya Bay Collaboration], "Improved Measurement of Electron Antineutrino Disappearance at Daya Bay", Chin. Phys. C **37** (2013) 011001 doi:10.1088/1674-1137/37/1/011001 [arXiv:1210.6327 [hep-ex]].

[25] "Cosmic Rays Underground", Section 28.4 *in* K. A. Olive *et al.* [Particle Data Group Collaboration], "Review of Particle Physics", Chin. Phys. C **38**, 090001 (2014).

[26] V. A. Kudryavtsev, "Muon simulation codes MUSIC and MUSUN for underground physics", Comput. Phys. Commun. **180**, 339 (2009) [arXiv:0810.4635].

[27] G. M. An *et al.* "A parametrization of the cosmic-ray muon flux at sea-level", [arXiv:1509.06176].

[28] The ERA-Interim database of the European Centre for Medium-Range Weather Forecasts, http://www.ecmwf.int/en/research/climate-reanalysis/era-interim (2016)

[29] D. P. Dee *et al.* "The ERA-Interim reanalysis: configuration and performance of the data assimilation system", Quarterly Journal of the Royal Meteorological Society Volume 137, Issue 656, pages 553-597, April 2011 Part A, doi:10.1002/qj.828

[30] E. W. Grashorn *et al.* "The Atmospheric charged kaon/pion ratio using seasonal variation methods", Astropart. Phys. **33**, 140 (2010) [arXiv:0909.5382].

[31] I. Durre *et al.*, "Overview of the Integrated Global Radiosonde Archive", ftp://ftp.ncdc.noaa.gov/pub/data/igra/v1/igra-overview.pdf (2005).

[32] T. K. Gaisser, "Cosmic rays and particle physics", Cambridge, UK: Univ. Pr. (1990) 279 p.

[33] G. D. Barr *et al.* "Uncertainties in Atmospheric Neutrino Fluxes," Phys. Rev. D **74**, 094009 (2006) [arXiv:astro-ph/0611266].

[34] P. Adamson *et al.* [MINOS Collaboration], "Measurement of the atmospheric muon charge ratio at TeV energies with MINOS," Phys. Rev. D **76**, 052003 (2007) [arXiv:0705.3815].

[35] R. Brun *et al.*, "ROOT - An Object Oriented Data Analysis Framework", Nucl. Inst. Meth. in Phys. Res. A 389 (1997) 81-86, See also http://root.cern.ch/.

[36] Numerical Recipes, The Art of Scientific Computing, Third Edition, p. 785, available online at http://apps.nrbook.com/empanel/index.html?pg=785#.

[37] V.N. Bakatanov *et al.* (Baksan Collaboration), "Energy spectrum of cascades generated by muons in Baksan underground scintillation telescope", 19th Intern. Cosmic Ray Conf., Vol. 8 p 36-38, http://adsabs.harvard.edu/abs/1985ICRC....8...36B